Association of Variable Star Observers, Cambridge, MA 02138, USA. [64]Astronomical Institute, Academy of Sciences of the Czech Republic, Ondrejov, Czech Republic. [65]Mullard Space Science Laboratory, University College London, Holmbury St. Mary, Dorking, Surrey, RH5 6NT, UK. [66]Sternberg Astronomical Institute, Moscow University, Moscow, Russia. [67]Dipartimento di Fisica "Enrico Fermi," Università di Pisa, Pisa I-56127, Italy. [68]Columbia Astrophysics Laboratory, Columbia University, New York, NY 10027, USA. [69]Catholic University of America, Washington, DC 20064, USA.

Supporting Online Material
www.sciencemag.org/cgi/content/full/329/5993/817/DC1
Materials and Methods
SOM Text
Figs. S1 to S6
Tables S1 to S3
References

19 May 2010; accepted 12 July 2010
10.1126/science.1192537

Quantum Oscillations and Hall Anomaly of Surface States in the Topological Insulator Bi_2Te_3

Dong-Xia Qu,[1]* Y. S. Hor,[2] Jun Xiong,[1] R. J. Cava,[2] N. P. Ong[1]*

Topological insulators are insulating materials that display massless, Dirac-like surface states in which the electrons have only one spin degree of freedom on each surface. These states have been imaged by photoemission, but little information on their transport parameters, for example, mobility, is available. We report the observation of Shubnikov–de Haas oscillations arising from the surface states in nonmetallic crystals of Bi_2Te_3. In addition, we uncovered a Hall anomaly in weak fields, which enables the surface current to be seen directly. Both experiments yield a surface mobility (9000 to 10,000 centimeter^2 per volt-second) that is substantially higher than in the bulk. The Fermi velocity of 4×10^5 meters per second obtained from these transport experiments agrees with angle-resolved photoemission experiments.

Recently, the existence of a new class of bulk insulators called topological insulators has been predicted (*1*–*6*). In a topological insulator, the bulk energy gap is traversed by surface states in which the spin of the electron is locked perpendicular to its momentum by strong spin-orbit interaction. On each surface, the electrons have only one spin degree of freedom (fixed helicity). The spin-resolved nature of the surface states has been confirmed in angle-resolved photoemission spectroscopy (ARPES) experiments on BiSb (*7*), Sb (*8*), Bi_2Se_3 (*9*), and Bi_2Te_3 (*10*). The spin locking in BiSb has also been studied by scanning tunneling microscopy (*11*). However, it has been a challenge to resolve the conductance of the surface states from the dominant bulk contribution (*12*, *13*). The lack of transport information, especially the mobility, is a serious hindrance. Moreover, detection of the surface currents is a crucial first step in the investigation of phenomena, such as the Majorana fermion (*5*) and unconventional electrodynamics (*6*), in topological insulators.

We report dual evidence for surface state conduction in Bi_2Te_3 from Shubnikov–de Haas (SdH) oscillations and from the weak-field Hall effect. As in the case of the selenide Bi_2Se_3 (*12*), as-grown crystals of Bi_2Te_3 usually display a metallic resistivity ρ versus temperature *T* (in Bi_2Te_3, the Fermi energy E_F lies in the valence band VB). By selective cleaving of many crystals from a boule of Bi_2Te_3 grown with a weak compositional gradient (*14*), we have obtained nonmetallic crystals (Fig. 1A). In the nonmetallic samples Q1, Q2, and Q3, ρ rises when *T* is lowered below 150 K and saturates to values 4 to 5 mohm cm at 4 K or ~50 times larger than the value in the metallic sample N1. The surface state dispersion obtained by ARPES (*10*) is sketched in Fig. 1B, with E_F in our samples indicated. Even in the most resistive sample Q3, the bulk conductance is ~300 times larger than the surface term (see below). Nonetheless, the latter may be resolved by detecting the SdH oscillations in the resistivity and the Hall resistivity ρ_{yx} at low *T*. Quantum oscillations are well resolved in the raw trace of the Hall conductivity $\sigma_{xy} = \rho_{yx}/(\rho_{xx}^2 + \rho_{yx}^2)$ measured at $T = 0.3$ K (Fig. 1, C and D). In metals, SdH oscillations correspond to successive emptying of Landau levels (LL) as the magnetic field *H* is increased. The LL index *n* is related to the extremal cross section S_F of the Fermi surface (FS) by

$$2\pi(n+\gamma) = S_F\frac{\hbar}{eB} \qquad (1)$$

where $\gamma = 0$ or ½, *e* is the electron charge, *h* is Planck's constant ($\hbar = h/2\pi$), and *B* is the magnetic flux density.

For a two-dimensional (2D) FS, the peak positions depend only on the field component $H_\perp = H\cos\theta$ along the axis **c** normal to the cleavage plane (θ is the tilt angle between **H** and **c**). To

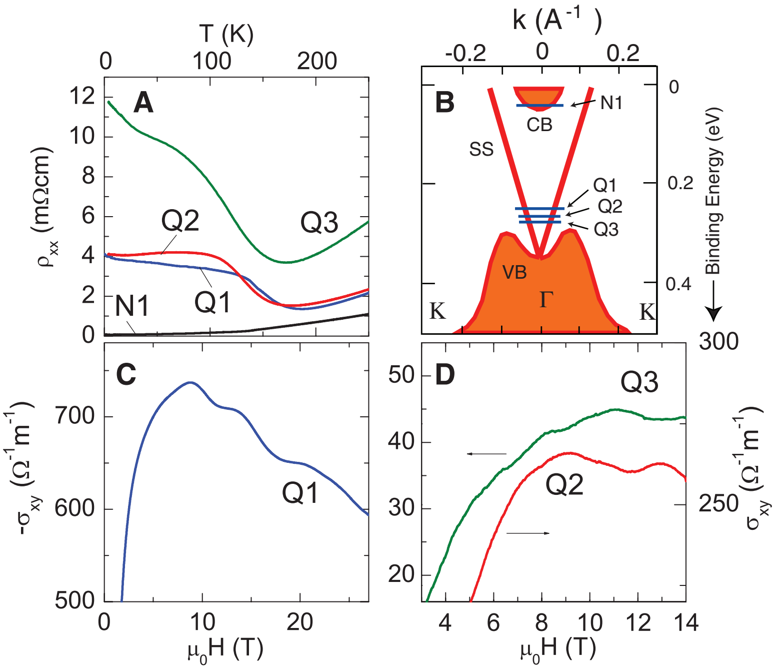

Fig. 1. (**A**) The resistivity profiles ρ versus temperature *T* of samples Q1, Q2, Q3, and N1. (**B**) Sketch of the surface state dispersion near the Γ point [traced from (*10*)]. The Fermi energies of samples Q1, Q2, Q3, and N1 are indicated by short lines (CB, conduction band). Curves of the Hall conductivity σ_{xy} versus the magnetic field *H* in sample Q1 (**C**) and in samples Q2 and Q3 (**D**) showing well-resolved SdH oscillations. μ_0 is the permeability.

---

[1]Department of Physics, Princeton University, Princeton, NJ 08544, USA. [2]Department of Chemistry, Princeton University, Princeton, NJ 08544, USA.

*To whom correspondence should be addressed. E-mail: dqu@princeton.edu (D.-X.Q.); npo@princeton.edu (N.P.O.)

test this hypothesis, we tracked how the SdH extrema shift with θ, in fields up to 30 T [supporting online material (SOM) section S2]. We compare the derivative $d\rho_{xx}/dH$ in nonmetallic Q1 with that in the metallic sample N1 (Fig. 2, A and B, respectively). In sample Q1, the period of the oscillations depends only on $H_\perp$: The magnetic field corresponding to the $n = 3$ minimum varies with θ as 1/cosθ up to 65° (Fig. 1C). For 65° < θ < 90°, the oscillations are not resolved. By contrast, the oscillations in N1 survive up to θ = 90° (Fig. 1B). As θ → 90°, S_F in N1 deviates strongly from the 1/cosθ trend, to saturate at a value ~1.5× larger than that at θ = 0. From the comparison, we conclude that the quantum oscillations in the nonmetallic sample arise from a 2D FS (SOM section S2).

To extract more specific information on the surface states, we next analyzed how the SdH amplitudes vary with T in samples Q2 and Q3 (measured with **H**||**c**). As shown in Fig. 3A, the oscillation amplitudes in $d\rho_{xx}/dH$ decrease rapidly as T is raised from 0.3 to 20 K. Although measurements were not carried out at intermediate θ in Q2 and Q3, we verified that the SdH peaks were absent at θ = 90°. In the index plot (Fig. 3B), we confirmed that the (inverse) peak fields $1/B$ fall on a straight line versus the integers n (Eq. 1). For Q2 and Q3, the slopes yield $S_F = 33.3$ and 28.6 T, with Fermi wave vector $k_F = 0.032$ and 0.030 Å^{-1}, respectively (Table 1). In Q1, the shallower slope yields $k_F = 0.036$ Å^{-1}. Extrapolation of the high-field SdH peaks in Q1 is consistent with $0 < \gamma < ½$ (figs. S3 and S4). To find the corresponding E_F, we next determine the Fermi velocity v_F.

The T dependence of the amplitude $\Delta\sigma_{xx}$ of conductivity oscillations is given by $\Delta\sigma_{xx}(T) = \Delta\sigma_{xx}(0)\lambda(T)/\sinh\lambda(T)$. For 2D massless Dirac states, the thermal factor $\lambda(T)$ is given by (*15*, *16*)

$$\lambda(T) = \frac{2\pi^2 k_B T}{\hbar e B} m_{cyc} \qquad (2)$$

where k_B is Boltzmann's constant and $m_{cyc} = E_F/v_F^2$ is the cyclotron mass. In low H, the degree of orbit bending is measured by the Hall mobility μ, given by $\mu = e\tau_{tr}/m_{cyc} = e\ell/\hbar k_F$, where τ_{tr} and ℓ are the transport lifetime and mean free path, respectively. We may find m_{cyc} by fitting the T dependence of the conductivity amplitudes to Eq. 2 (Fig. 3D). Because k_F is known, we calculate $v_F = 3.7$ and 4.2×10^5 m s^{-1} for Q2 and Q3, respectively [from ARPES (*10*), $v_F \sim 4 \times 10^5$ m s^{-1}]. Lastly, this yields $E_F = 94$, 84, and 78 meV above the Dirac point in samples Q1, Q2, and Q3, respectively (Fig. 1B).

The lifetime τ of the surface states can be found by estimating the Dingle factor e^{-D}, where $D = 2\pi^2\Gamma E_F/(\hbar e B v_F^2)$, with Γ = 1/τ the scattering rate. Because $\Delta R/R_0 \sim \frac{\lambda(T)}{\sinh\lambda(T)} e^{-D}$ (where R is resistance), we may find Γ from the slope in the semilog plot of $(\Delta R/R_0)B\sinh\lambda(T)$ versus $1/B$ (Fig. 3, E and F). We find that $v_F\tau = 217$ and 219 nm in Q2 and Q3, respectively (these values are lower bounds for the mean free path $\ell = v_F\tau_{tr}$ because $\tau_{tr} > \tau$ in principle). The metallicity parameter is then $k_F\ell > 69$ and 66 in samples Q2 and Q3, respectively.

The conductance tensor $G_{ij}(B)$ of the 2D Dirac gas may be calculated in the semiclassical Boltzmann approximation (*14*). Defining $G(B) \equiv G_{xx}(B)$, we may express the zero-B con-

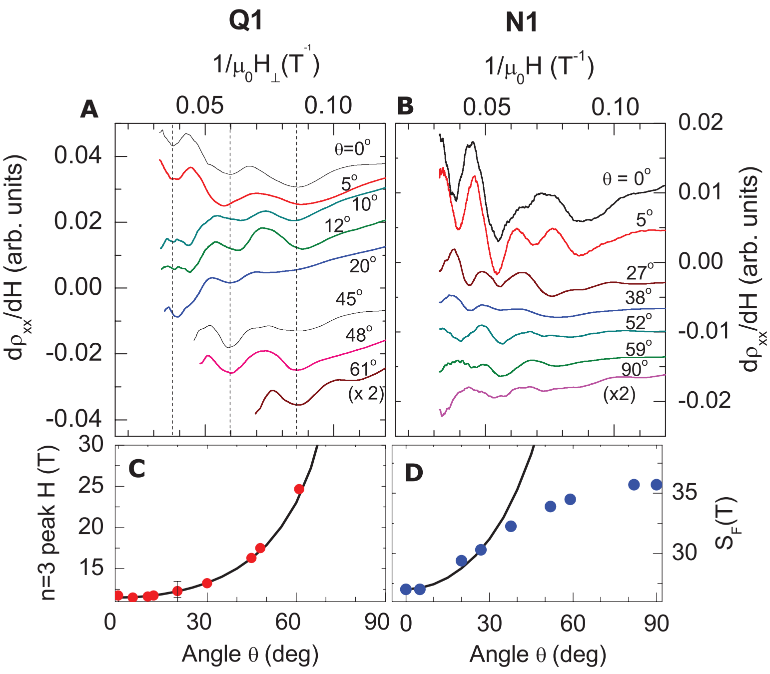

Fig. 2. The resistivity derivative $d\rho_{xx}/dH$ versus $1/H_\perp = 1/(H\cos\theta)$ in (**A**) sample Q1 and (**B**) sample N1 at selected tilt angles θ. In (A), the minima lie on the vertical dashed lines consistent with a 2D FS, whereas in (B), the minima shift systematically with θ. (**C**) The field position of the $n = 3$ LL peak for sample Q1 (red circles) varies with θ as 1/cosθ (black curve), consistent with a 2D FS. (**D**) The period S_F for sample N1 (blue circles) increases by 35% as θ → 90°, deviating strongly from 1/cosθ (black curve), consistent with a 3D FS.

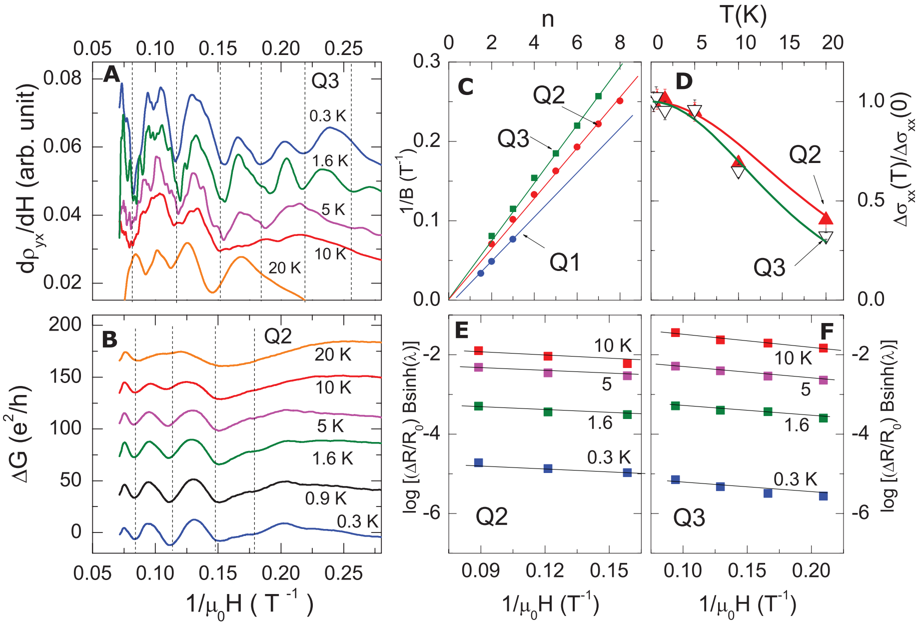

Fig. 3. (**A**) Derivative $d\rho_{yx}/dH$ versus $1/H$ in sample Q3 measured at temperatures T between 0.3 and 20 K. (**B**) ΔG (conductance obtained after subtracting a smooth background based on curves measured above 20 K) for sample Q2 at selected T over the same interval. (**C**) LL index plot $1/B$ versus n for samples Q1, Q2, and Q3. Our results are consistent with $0 < \gamma < ½$ (fig. S3). Values of S_F and k_F derived are reported in Table 1. (**D**) T dependence of the normalized conductivity amplitude $\Delta\sigma_{xx}(T)/\Delta\sigma_{xx}(0)$ at 0.3 K in samples Q2 (with H = 12 T) and Q3 (7.8 T). The curves are best fits to $\lambda(T)/\sinh\lambda(T)$ (Eq. 2). Dingle plots of $\log[(\Delta R/R_0)B\sinh\lambda]$ versus $1/H$, used to determine τ and $v_F\tau$ for (**E**) sample Q2 and (**F**) sample Q3.

ductance as $G(0) = (e^2/h)k_F\ell$, whereas the Hall conductance is

$$G_{xy} = \frac{2\pi e^3}{h^2}\frac{B\ell^2}{[1+(\mu B)^2]} \qquad (3)$$

(including both spin degrees). With $k_F\ell \sim 70$, we calculate $G(0) \approx 2.4 \times 10^{-3}$ ohm^{-1}, compared with the observed total resistance $R \approx 1.4$ ohm at 0.3 K in sample Q1. Hence, the 2D states account for ~0.3% of the total conductance observed at 0.3 K. Interestingly, the large value of $k_F\ell$ implies a large Hall mobility ($\mu = 10{,}200$ cm^2 V^{-1} s^{-1}). In weak H, the surface Hall current may dominate the low-mobility bulk Hall current.

We next report the detection of this surface Hall current as a distinct anomaly. In Fig. 4A, we plot the observed Hall conductivity σ_{xy} in sample Q3. In addition to the SdH oscillations in high fields (>5 T), we observe a prominent "dispersive" anomaly in weak H corresponding to a high-mobility contribution that is n-type. We express the observed Hall conductivity as the sum

$$\sigma_{xy} = \sigma^{b}_{xy} + \frac{G_{xy}}{t} \qquad (4)$$

where $\sigma^{b}_{xy} > 0$ is the bulk, p-type Hall conductivity and $G_{xy} < 0$ the surface Hall conductance given in Eq. 3, with t the crystal thickness. As shown in Fig. 1C and D, the sign of ρ_{yx} in sample Q1, fixed by the bulk carriers, is n-type, whereas Q2 and Q3 are p-type (fig. S4 and SOM section S4). By using Eq. 3 and a Drude-like expression for σ^{b}_{xy}, we have achieved a close fit to the nonmonotonic curve in Fig. 4A (fig. S5).

On subtracting σ^{b}_{xy}, we isolate the surface term G_{xy}, which shows a large dispersive anomaly centered at $H = 0$, with quantum oscillations in the wings (Fig. 4B). The solid curve is the fit to Eq. 3 (the semiclassical expression does not describe the quantum oscillations). By Eq. 3, G_{xy} attains the maximum value $G^{max}_{xy} = (e^2/2h)k_F\ell$ at the peak field $B_p = 1/\mu$ (arrows in Fig. 4B). From the fit, we find $\mu \sim 9000$ cm^2 V^{-1} s^{-1}, $k_F\ell = 94$, $k_F = 0.04$ Å^{-1}, and $\ell = 235$ nm. Given the nonuniformity of the cross-section and the uncertainties in measuring t and the voltage lead spacing L (both ± 10%), these are in good agreement with the numbers inferred from the SdH period and the Dingle analysis (*17*).

Table 1. Parameters in samples Q1, Q2, Q3, and N1. S_F and k_F are determined from the SdH period. E_F and v_F are obtained from the T dependence of the amplitude $\Delta\sigma_{xx}(T)/\Delta\sigma_{xx}(0)$. ℓ is found from the Dingle factor e^{-D}. The length (L), width (W), and thickness (t) are in µm. The uncertainty in v_F is ±10%. Dash entries indicate quantities not measured.

units	S_F T	k_F Å^{-1}	E_F meV	$k_F\ell$ –	v_F 10^5 m s^{-1}	$L \times W \times t$ µm^3
Q1	41.7	0.036	94	–	–	650 × 850 × 100
Q2	33.3	0.032	84	69	3.7	1500 × 1200 × 150
Q3	28.6	0.030	78	66	4.2	700 × 1060 × 140
N1	23.3*	0.027	–	–	–	700 × 730 × 40

*measured at θ = 0.

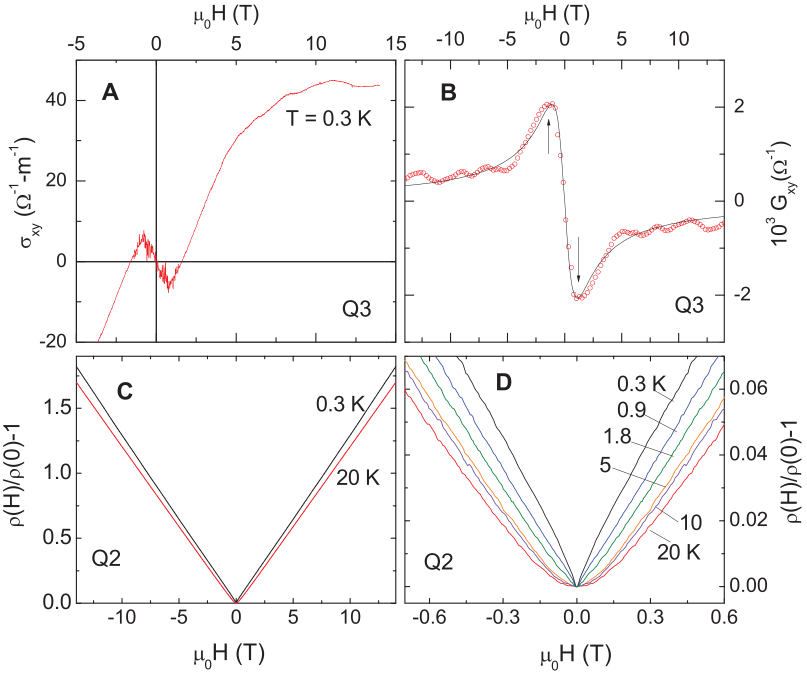

Fig. 4. (**A**) The Hall conductivity σ_{xy} versus H in Q3 measured at 0.3 K, showing quantum oscillations above 5 T and a dispersive anomaly in weak H. (**B**) Surface Hall conductance G_{xy} obtained by subtracting the bulk contribution σ^{b}_{xy} (Eq. 4). The solid curve is the fit to G_{xy} in Eq. 3 (details in SOM section S5). The peak field B_p (arrows) gives $1/\mu$, whereas the maximum value yields $(e^2/2h)k_F\ell$. (**C**) The linear MR measured with **H**||**c** at 0.3 and 20 K ($\rho \equiv \rho_{xx}$). (**D**) Rounding of the nonanalytic cusp at $H = 0$ in increasing T.

The quantitative agreement with 2D states persuades us that the weak-field Hall anomaly originates from Dirac surface states. Because of the large difference in mobilities and the difference in carrier sign, we are able to resolve directly the surface Hall current as the dispersive anomaly superposed on the bulk Hall current. The curve in Fig. 4B is a snapshot of the Dirac surface current from which μ and $k_F\ell$ may be estimated by inspection.

By how much is μ enhanced over the bulk? Unfortunately, in the nonmetallic crystals, it is not straightforward to pin down the hole density p and mobility μ_b of the bulk states. The bulk Hall signal changes sign abruptly as E_F approaches the Dirac point. As shown in fig. S1, samples Q1 and N1 are n-type, whereas Q2 and Q3 are p-type. This suggests competition and compensation between electron and hole bulk bands. A more interesting complication is the unusual magnetoresistance (MR). In samples Q1, Q2, and Q3, the transverse MR measured with **H**||**c** displays a highly unusual linear increase versus H [by contrast, metallic crystals do not show the linear MR (fig. S2)]. As shown in Fig. 4C (for sample Q2), the nonanalytic variation $\frac{\rho(H)}{\rho(0)} - 1 \sim |H|$ extends over 3.5 decades in H (from 30 G to 14 T) at 0.3 K. The expanded view in Fig. 4D shows that, as T is raised to 20 K, the low-H region is rounded. The large linear MR is predominantly caused by coupling of the spin to H. When H is aligned with the current, the longitudinal MR is 50% as large as the transverse MR (fig. S7). This unusual MR, which may arise from a spin-mediated decrease in the bulk carrier density p with H, implies that the bulk states cannot be regarded as conventional impurity bands. However, if we use the bulk value obtained from the fit in Fig. 4B ($\mu_b \sim 860$ cm^2 V^{-1} s^{-1}), we find that the surface mobility is 12 times larger than the bulk value.

By using both the SdH and weak-field Hall anomaly, we have resolved a surface current that is n-type with $k_F \sim 0.035$ Å^{-1} and a velocity $v_F \sim 4 \times 10^5$ m s^{-1}. The observed mobility and $k_F\ell$ are enhanced substantially over the bulk values. These features are consistent with protected surface Dirac states. With the surface current detected, research on topological insulators may now be expanded to include transport experiments.

References and Notes

1. L. Fu, C. L. Kane, E. J. Mele, *Phys. Rev. Lett.* **98**, 106803 (2007).
2. L. Fu, C. L. Kane, *Phys. Rev. B* **76**, 045302 (2007).
3. J. E. Moore, L. Balents, *Phys. Rev. B* **75**, 121306 (2007).
4. B. A. Bernevig, T. L. Hughes, S.-C. Zhang, *Science* **314**, 1757 (2006).
5. L. Fu, C. L. Kane, *Phys. Rev. Lett.* **100**, 096407 (2008).
6. X. L. Qi, T. L. Hughes, S. C. Zhang, *Phys. Rev. B* **78**, 195424 (2008).

7. D. Hsieh *et al.*, *Nature* **452**, 970 (2008).
8. D. Hsieh *et al.*, *Science* **323**, 919 (2009).
9. Y. Xia *et al.*, *Nat. Phys.* **5**, 398 (2009).
10. Y. L. Chen *et al.*, *Science* **325**, 178 (2009); published online 11 June 2009 (10.1126/science.1173034).
11. P. Roushan *et al.*, *Nature* **460**, 1106 (2009).
12. J. G. Checkelsky *et al.*, *Phys. Rev. Lett.* **103**, 246601 (2009).
13. A. A. Taskin, Y. Ando, *Phys. Rev. B* **80**, 085303 (2009).
14. Materials and methods are available as supporting material on *Science* Online.
15. K. S. Novoselov *et al.*, *Nature* **438**, 197 (2005).
16. V. P. Gusynin, S. G. Sharapov, *Phys. Rev. B* **71**, 125124 (2005).
17. We may exclude the interpretation of G_{xy} as a bulk term as follows. If we write G_{xy}/t as $n'e\mu^2B/[1 + (\mu B)^2]$ with μ fixed at 10,000 cm^2 V^{-1} s^{-1}, we get a bulk density $n' = 1.4 \times 10^{14}$ cm^{-3}. This tiny 3D FS pocket would have a Fermi cross section S_F' that is far too small, by a factor of 360, to match the SdH period (the wave vector $k'_F = 1.6 \times 10^{-3}$ $Å^{-1}$ is 19 times too small).

18. The research is supported by NSF under Materials Research Science and Engineering Centers grant DMR-0819860. We acknowledge valuable comments by J. G. Checkelsky, M. Z. Hasan, A. Yazdani, A. Bernevig, and F. D. M. Haldane. High-field measurements were carried out at the National High Magnetic Field Laboratory, Tallahassee, which is supported by NSF cooperative agreement no. DMR-0084173, by the state of Florida, and by the U.S. Department of Energy.

Supporting Online Material

www.sciencemag.org/cgi/content/full/science.1189792/DC1
Materials and Methods
SOM sections S1 to S6
Figs. S1 to S9

18 March 2010; accepted 12 July 2010
Published online 29 July 2010;
10.1126/science.1189792
Include this information when citing this paper.

In-Plane Resistivity Anisotropy in an Underdoped Iron Arsenide Superconductor

Jiun-Haw Chu,[1,2] James G. Analytis,[1,2] Kristiaan De Greve,[3] Peter L. McMahon,[3] Zahirul Islam,[4] Yoshihisa Yamamoto,[3,5] Ian R. Fisher[1,2]*

High-temperature superconductivity often emerges in the proximity of a symmetry-breaking ground state. For superconducting iron arsenides, in addition to the antiferromagnetic ground state, a small structural distortion breaks the crystal's C_4 rotational symmetry in the underdoped part of the phase diagram. We reveal that the representative iron arsenide $Ba(Fe_{1-x}Co_x)_2As_2$ develops a large electronic anisotropy at this transition via measurements of the in-plane resistivity of detwinned single crystals, with the resistivity along the shorter *b* axis ρ_b being greater than ρ_a. The anisotropy reaches a maximum value of ~2 for compositions in the neighborhood of the beginning of the superconducting dome. For temperatures well above the structural transition, uniaxial stress induces a resistivity anisotropy, indicating a substantial nematic susceptibility.

The iron-arsenide family of compounds appears to present a new paradigm for high-temperature superconductivity. The parent compounds are multiband itinerant antiferromagnets (*1*, *2*) with a Fermi surface consisting of several small pockets resulting from reconstruction due to the broken translational symmetry (*3*, *4*). Suppression of the antiferromagnetic ground state by various means eventually leads to superconductivity, with critical temperatures of up to 55 K (*5*). Notably, the antiferromagnetic transition is always preceded by or coincident with a tetragonal to orthorhombic structural distortion (*6*–*8*). It has been proposed that this structural distortion is driven by an electronic phase transition (*9*–*12*), perhaps due to orbital ordering (*13*–*16*) or fluctuating antiferromagnetism (*9*, *10*). In both proposals, a large in-plane electronic anisotropy is anticipated in the "nematic" state (*17*).

Although electron nematic phases have been intensively studied in quantum Hall systems (*18*) and in $Sr_3Ru_2O_7$ (*19*), there is growing evidence for substantial electronic anisotropy in underdoped cuprates (*20*, *21*) that cannot be explained by the structural orthorhombicity alone. In particular, the recent observation of a large in-plane anisotropy in the Nernst effect in $YBa_2Cu_3O_{7-\delta}$ suggests that the much-debated pseudogap phase is a rotational symmetry-breaking phase (*22*). The crucial experiments in all of these cases probe the in-plane transport anisotropy that arises due to the nematic order (*17*). Here, we report measurements of in-plane resistivity anisotropy of $Ba(Fe_{1-x}Co_x)_2As_2$ over a wide range of doping and temperature, to elucidate the nature of the structural phase transition in the iron pnictides.

One difficulty with probing the in-plane electronic anisotropy of the iron arsenides is that the material naturally forms dense structural twins below the orthorhombic transition at T_S (Fig. 1, A and B) (*23*). Measurements of twinned samples present only an average of the intrinsic anisotropy, from which little detailed information can be extracted. For the present study, we have developed a mechanical cantilever device (shown in Fig. 1 C) that is able to detwin crystals in situ. Crystals were cut such that the orthorhombic *a* and *b* axes were aligned parallel to the direction of applied stress. With only modest pressures

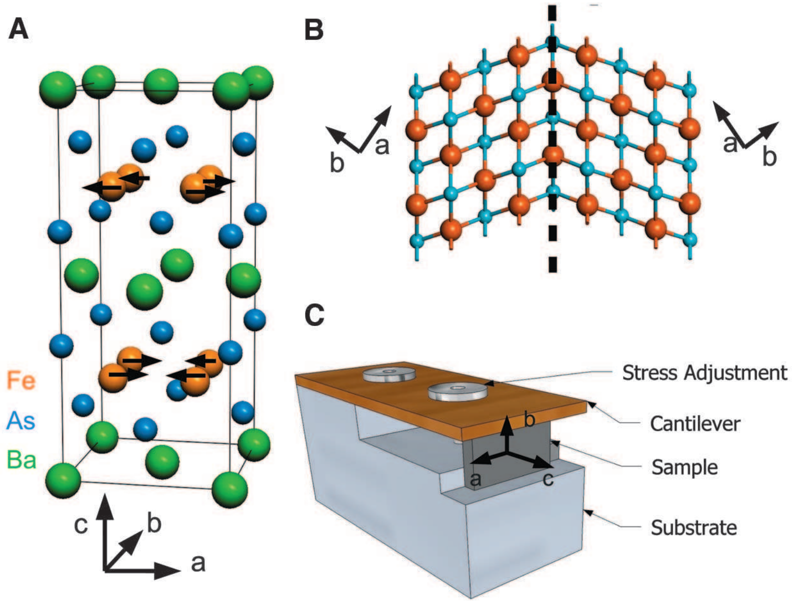

Fig. 1. (**A**) Diagram of the crystal structure of $BaFe_2As_2$ in the antiferromagnetic state. The magnetic moments on the iron sites point in the *a* direction and align antiparallel along the longer *a* axis and parallel along the shorter *b* axis. (**B**) Diagram illustrating a twin boundary between two domains that form on cooling through the structural transition at T_S. Dense twinning in macroscopic crystals obscures any in-plane electronic anisotropy in bulk measurements. (**C**) Diagram of the device used to detwin single crystals in situ. The sample is held sandwiched between a cantilever and a substrate, with a screw in the center of the cantilever to adjust the uniaxial pressure. The (0 0 1) surface of the crystal is exposed, enabling transport measurements.

---

[1] Department of Applied Physics and Geballe Laboratory for Advanced Materials, Stanford University, Stanford, CA 94305, USA. [2] Stanford Institute of Energy and Materials Science, SLAC National Accelerator Laboratory, 2575 Sand Hill Road, Menlo Park, CA 94025, USA. [3] E. L. Ginzton Laboratory, Stanford University, Stanford, CA 94305, USA. [4] The Advanced Photon Source, Argonne National Laboratory, Argonne, IL 60439, USA. [5] National Institute of Informatics, Hitotsubashi 2-1-2, Chiyoda-ku, Tokyo 101-8403, Japan.

*To whom correspondence should be addressed. E-mail: irfisher@stanford.edu